Intermetallics 187 (2025) 109009

Contents lists available at ScienceDirect

Intermetallics

journal homepage: www.elsevier.com/locate/intermet

Integrated design of superhydrophobic structures and photocatalytic functions of $Zr_{46}Cu_{46}Al_8$ metallic glass surfaces

Guanzhong Ding [a], Guoyang Zhang [b,*], Ranfeng Wei [b], Yujia Wang [a], Rui Zheng [a], Qijing Sun [b], Jingwang Lv [b], Haipeng Wang [b], Dan Li [c], Paul K. Chu [c], Li Liu [a,**], Xiangjin Zhao [b,***]

[a] School of Environmental and Material Engineering, Yantai University, Yantai, 264005, China
[b] Yantai Key Laboratory of Advanced Nuclear Energy Materials and Irradiation Technology, College of Nuclear Equipment and Nuclear Engineering, Yantai University, Yantai, 264005, China
[c] Department of Physics, Department of Materials Science and Engineering, and Department of Biomedical Engineering, City University of Hong Kong, Kowloon, Hong Kong, China

ARTICLE INFO

Keywords:
Metallic glasses
Superhydrophobic surfaces
Electrochemical evaluation
Corrosion resistance
Photocatalytic properties

ABSTRACT

Metallic glasses have considerable potential in applications such as wastewater degradation, but the corrosion resistance and catalytic degradation performance require improvement. Herein, this study presents a simple electrochemical strategy that simultaneously improves the superhydrophobic properties of the cathode and anode surfaces by using $Zr_{46}Cu_{46}Al_8$ metallic glass as the cathode and anode substrates. The etched surface on the anode comprises a micro-nanometer composite coating of $ZrO_2/CuO/Cu_2O$, while the cathode surface has a micro-nanometer composite structure of $CuO/Cu_2O/Fe_2O_3$. The composite oxides produce enhanced catalytic degradation characteristics on the substrate. The micro-nanometer structures formed on the metallic glass surface give rise to superhydrophobicity, which improves the corrosion resistance and adaptability to complex environments. Furthermore, the stability and cyclic degradation capability are excellent, boding well for industrial implementation. Our results reveal a novel strategy to improve both the structure and functions of metallic glasses for different applications such as wastewater treatment.

1. Introduction

Metallic glasses (MGs) have the characteristics of short-range order and long-range disorder, thus endowing them with excellent physical and chemical properties, especially in the field of catalysis [1–3]. The atomic arrangement on the surface of MG is irregular and in a metastable state with a high Gibbs free energy and a large number of highly active sites [4]. These sites are capable of adsorbing and degrading pollutants. Nevertheless, the catalytic efficiency reported so far is insufficient, and the stability and corrosion resistance are relatively poor [5,6]. It is thus important to improve both the structure and functions of MGs by optimizing the alloy composition, improving the kinetics by surface treatment [7], and altering the surface morphology to increase the reaction area. For example, Qin et al. [8] have prepared Co-based amorphous alloy powder by ball milling, and the powder can degrade acid orange II solutions faster than Fe-based MGs and Fe^0 metal powder. Wang et al. [5] have reported the degradation of organic water pollutants such as azo dyes by Mg-Zn MGs powder with an efficiency higher than that of the Mg-Zn crystalline powder in complex environments. However, the recycle of powder waste is difficult, and a supporting structure is required. Another method is to increase the active sites through various methods such as dealloying. Deng et al. [9] have prepared nanoporous Cu with an adjustable pore size (20–50 nm) by dealloying $Mg_{65}Cu_{25}Gd_{10}$ MGs in H_2SO_4. Compared with Mg-based MGs, the degradation rate increases by 2–4 times. Liu et al. [10] have prepared three-dimensional nanoporous copper catalysts by 3D printing and chemical dealloying. The degradation efficiency for azo dyes is 14 times higher than that of commercial Cu^{2+} and 4 times better than that of the Cu^0 powder. However, processing methods such as dealloying usually destroy the special disordered structure of MGs, consequently reducing its corrosion resistance, stability, and lifetime [9,11,12].

It is challenging to improve the catalytic degradation efficiency and

* Corresponding author.
** Corresponding author.
*** Corresponding author.
E-mail addresses: zhangguoyang@ytu.edu.cn (G. Zhang), liuli1980@ytu.edu.cn (L. Liu), zl2915@ytu.edu.cn (X. Zhao).

https://doi.org/10.1016/j.intermet.2025.109009
Received 1 July 2025; Received in revised form 18 September 2025; Accepted 21 September 2025

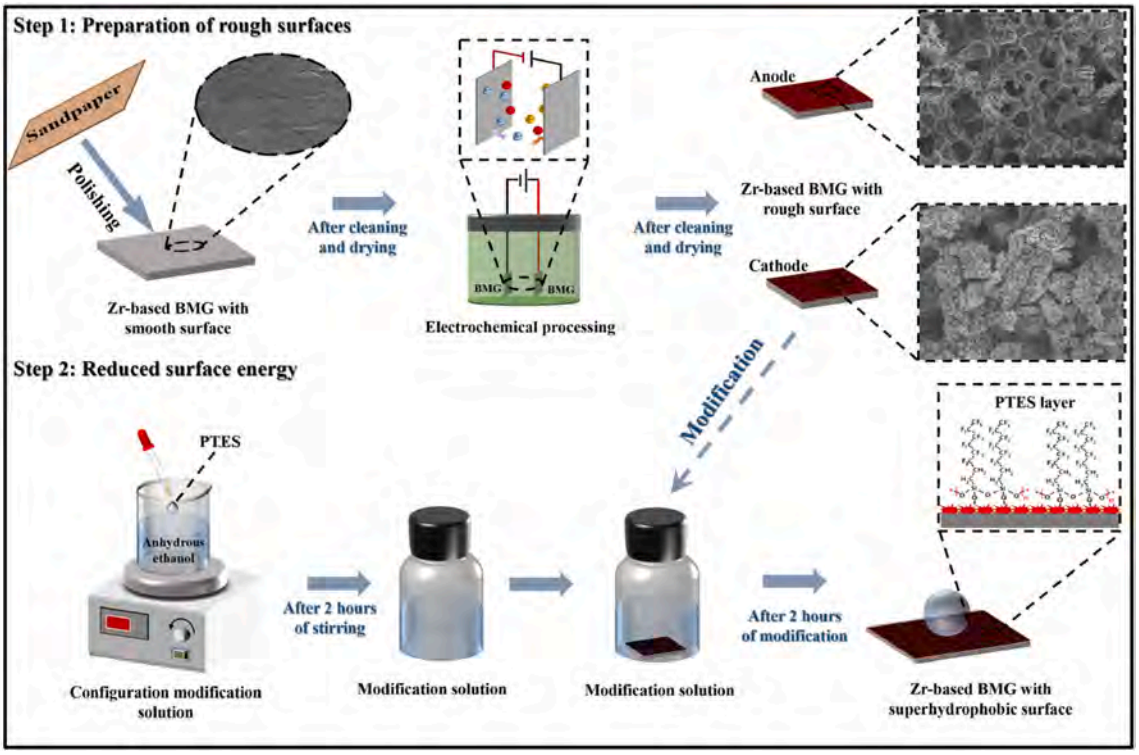

Fig. 1. Schematic diagram of the fabrication of superhydrophobic Zr-based BMG.

corrosion resistance of amorphous alloys. Inspired by the superhydrophobic structures of the surfaces of organisms and plants in nature, superhydrophobic surfaces have been shown to enhance the corrosion resistance of materials and produce self-cleaning properties [13,14]. Electrochemical machining (ECM) is one of the common techniques to produce superhydrophobic surfaces with high efficiency and repeatability [15]. Compared with other dealloying methods, ECM is not only simple and efficient but also can produce superhydrophobicity and surface self-cleaning properties. If superhydrophobic structures can be prepared on amorphous alloys such as MGs, the mechanical properties can be preserved while the issue of reduced corrosion resistance caused by dealloying can be mitigated [16].

In this work, an electrochemical method was devised for the $Zr_{46}Cu_{46}Al_8$ bulk metallic glass (BMG), where both the anode and cathode samples were concurrently electrochemically etched and electrochemically deposited within a single electrochemical processing procedure. Superhydrophobic structures are produced on the anode and cathode surfaces of BMG. During the electrochemical process, semiconducting oxides with distinct properties are fabricated to enhance the catalytic degradation on the MG surface. The superhydrophobicity, corrosion resistance, photocatalytic properties, and stability of the surfaces are investigated systematically. The strategy of integrating superhydrophobicity on both the anode and cathode of BMG compensates for the deficiency of powder catalysts and dealloyed catalysts, resulting in better structures and functions.

2. Experimental methods

2.1. Preparation of superhydrophobic structures

$Zr_{46}Cu_{46}Al_8$ BMG was fabricated by the water-cooled copper mold suction casting approach, where the purities of Zr, Cu, and Al raw materials exceeded 99.9 wt%. The dimensions of the $Zr_{46}Cu_{46}Al_8$ BMG substrate were 10 mm × 10 mm × 1.5 mm. The substrate surface was polished smooth using silicon carbide sandpaper and ultrasonically cleansed in deionized water and alcohol. Fig. 1 depicts the concurrent electrochemical etching and electrochemical deposition of $Zr_{46}Cu_{46}Al_8$ BMG within the same electrolytic cell under ultrasonic conditions at 40 °C for the preparation of superhydrophobic surfaces. Both the anode and cathode substrates were $Zr_{46}Cu_{46}Al_8$ BMG. The electrolyte was composed of $CuCl_2{\cdot}2H_2O$ (0.1 mol/L), $FeCl_3{\cdot}6H_2O$ (0.05 mol/L), and $C_8H_{11}NO_2$ (6.5 mmol/L), and the pH value was adjusted to 9 by adding 4 mol/L NaOH solution. The electrode spacing was 5 mm, and the reaction current density was 0.50 A/cm^2. The ultrasonic power was 40 W, and the frequency was 40 kHz. After the electrochemical treatment, the samples underwent modification treatment, including ultrasonic cleaning in deionized water and alcohol, followed by soaking in a 1.0 % 1H, 1H, 2H, 2H-perfluorooctyltriethoxysilane (PTES) ethanol solution for 2 h to reduce the surface energy.

2.2. Characterization

The contact angle (CA) and sliding angle (SA) were measured using a contact angle measuring instrument (JC2000C1, Zhongchen, China) with five independent measurements conducted for both parameters, and the average values were reported. Comprehensive characterization of surface microstructure and chemical composition was performed through scanning electron microscopy (SEM, JSM-7610F, JEOL, Japan) coupled with energy-dispersive spectroscopy (EDS), X-ray diffraction (XRD, Ultima IV, Rigaku, Japan), and X-ray photoelectron spectroscopy (XPS, Thermo Escalab 250, USA).

The corrosion resistance of superhydrophobic specimens was evaluated via potentiodynamic polarization measurements employing a three-electrode configuration: the superhydrophobic sample as working electrode, platinum as counter electrode, and saturated calomel electrode (SCE) as reference. Electrochemical tests were carried out in 3.5 wt % NaCl aqueous solution at a scan rate of 2 mV/s using an electrochemical workstation (CHI660E, Chenhua Instruments, China). UV resistance assessment was conducted under a 20 W ultraviolet lamp (λ = 253.7 nm) with a fixed irradiation distance of 20 cm. Mechanical durability was quantified by measuring the sliding distance of superhydrophobic specimens on 2000# silicon carbide sandpaper under 2

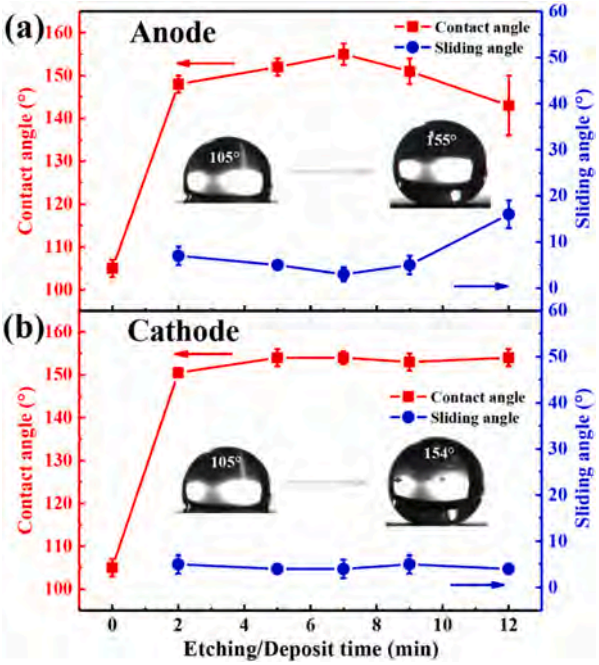

Fig. 2. The temporal evolution of CA and SA for surface-modified specimens: (a) Anode and (b) Cathode.

kPa normal load [3].

Photocatalytic decomposition performance was investigated by monitoring methyl orange (MO) degradation (10 mg/L, 4 mL) in the presence of H_2O_2 (30 wt%, 0.1 mL) under visible-light irradiation ($\lambda \geq$ 400 nm) from a 300 W Xe lamp. The reaction system maintained an irradiation intensity of 1.00 W/cm^2 at 30 °C with 15 cm light-source distance. Temporal concentration changes were tracked through UV–Vis spectrophotometry (UV-5500, Bio-Equip, China) by measuring absorbance variations of 3 mL aliquots at specific intervals. Antibacterial efficacy against Escherichia coli was assessed by immersing 1 × 1 cm^2 samples in 1 mL bacterial suspension (10^5 CFU/mL) for 1 h at 37 °C, followed by plating 100 μL aliquots on nutrient agar and incubating for 12 h at 37 °C prior to colony counting.

3. Results and discussion

3.1. Surface hydrophobicity and structures

During electrochemical processing, distinct surface reactions were observed between the anode and cathode amorphous specimens, with etching dominating at the anode and deposition prevailing at the cathode, where processing time served as the sole independent variable while contact angle (CA) and sliding angle (SA) measurements established the optimization criterion. Both cathode and anode specimens demonstrated optimal hydrophobicity when the processing duration reached 7 min, attaining CAs of 154° and 155° respectively. This phenomenon is systematically presented in Fig. 2, which depicts the temporal evolution of the CA and SA for the surface-modified specimens. Notably, the modified pristine amorphous substrate prior to electrochemical treatment displayed a CA of 105° ± 2°, and the water droplet

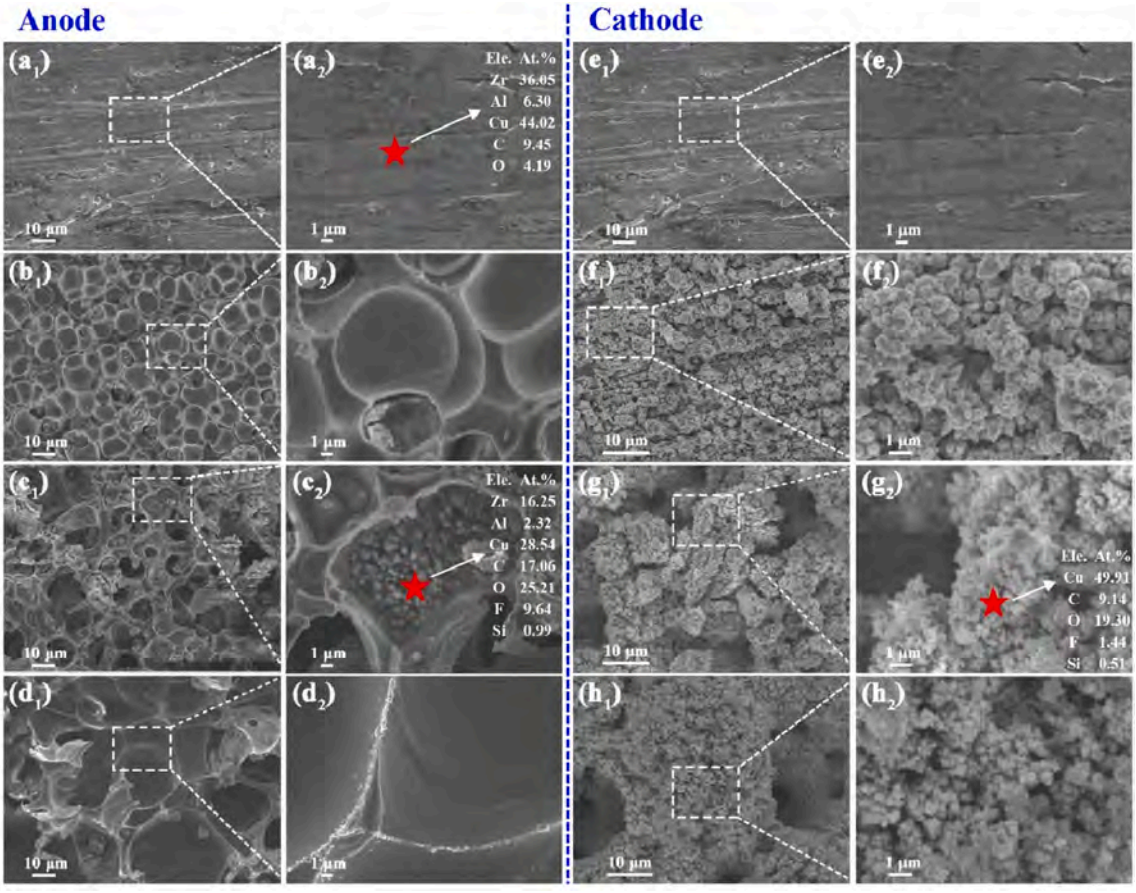

Fig. 3. Surface morphologies of the samples under different electrochemical processing times: (a) and (e) 0 min, (b) and (f) 2 min, (c) and (g) 7 min, (d) and (h) 12 min.

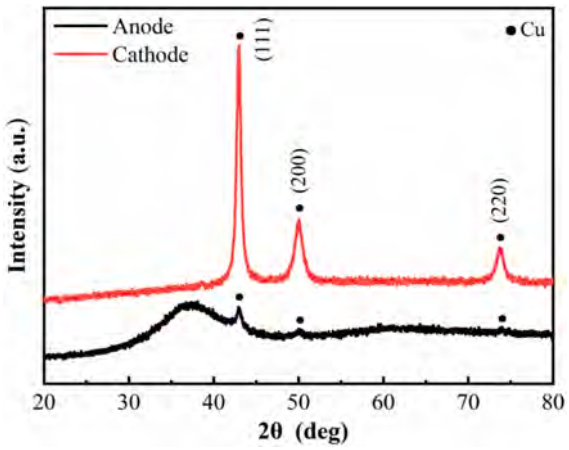

Fig. 4. XRD patterns of the sample surface after electrochemical processing at the optimal time.

adhered to the surface neither slid nor dropped. However, anode specimens demonstrated a monotonic CA increase with etching duration until reaching the critical 7 min threshold, beyond which progressive hydrophobicity decline occurred. It may be attributable to over-etching-induced structural degradation, though SA values maintained remarkable stability within 4.8° ± 0.3° throughout the 2–12 min processing window, suggesting preserved surface homogeneity despite competing mechanisms between hierarchical structure development and excessive material removal.

To clarify the correlation between electrochemical processing duration and hydrophobicity evolution, systematic morphological characterizations were conducted across varying preparation times. Fig. 3(a) presents the surface morphology of the modified pristine amorphous specimen. After 2 min of anode electrochemical etching, evenly distributed smooth corrosion pits appeared on the surface (Fig. 3(b)). Optimal surface architecture was achieved at 7-min processing, where honeycomb-like microstructures (Fig. 3(c1)) coexisted with evenly dispersed nano-scale protrusions (Fig. 3(c2)), corresponding to maximal CA values. When the etching process was extended to 12 min, it led to the enlargement of corrosion pits along with the complete erosion of nano-features (Fig. 3(d)), consequently diminishing surface hydrophobicity. Specimens processed for less than 7 min displayed smooth corrosion characteristics without hierarchical micro-nano composite structures. Nevertheless, they still retained sufficient air-trapping capability through surface pits to approach near-superhydrophobic states after modifying. Beyond the 7-min threshold, there was a progressive deterioration of the hierarchical architecture, which was directly associated with the decline in hydrophobicity. As a result, 7 min was established as the optimal duration for anode processing.

Contrastingly, Fig. 2 reveals minimal CA variation across cathode specimens with deposition time. To clarify this phenomenon, cathode surface structure evolution was examined through Fig. 3(f–h). Initial 2 min deposition generated uniform cauliflower-like micro-nano composite structures (Fig. 3(f)), which maintained their essential

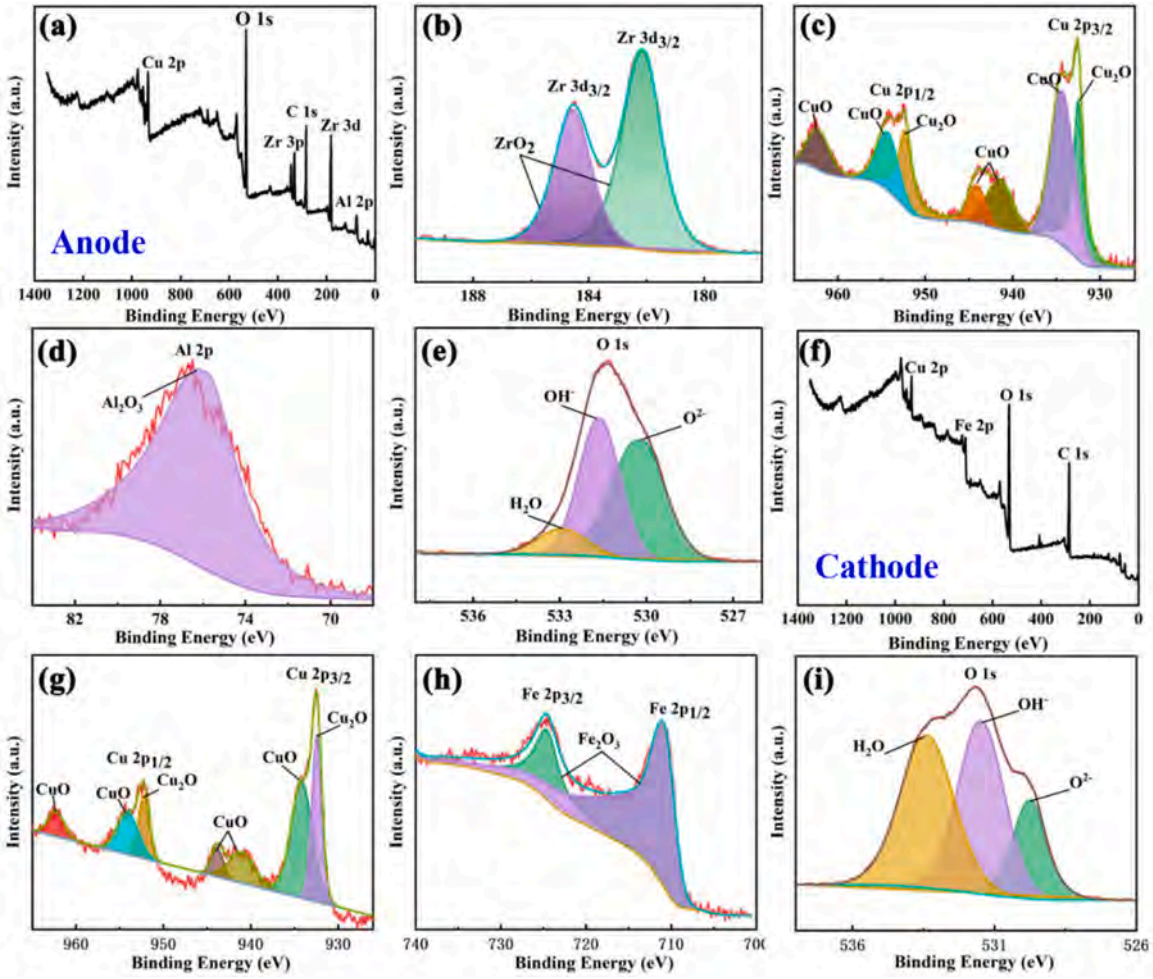

Fig. 5. XPS spectra of the anode after electrochemical treatment: (a) Survey spectrum, (b) Zr 3*d*, (c) Cu 2*p*, (d) Al 2*p*, (e) O 1*s*; XPS spectra of the cathode: (f) Survey spectrum, (g) Cu 2*p*, (h) Fe 2*p*, and (i) O 1*s*.

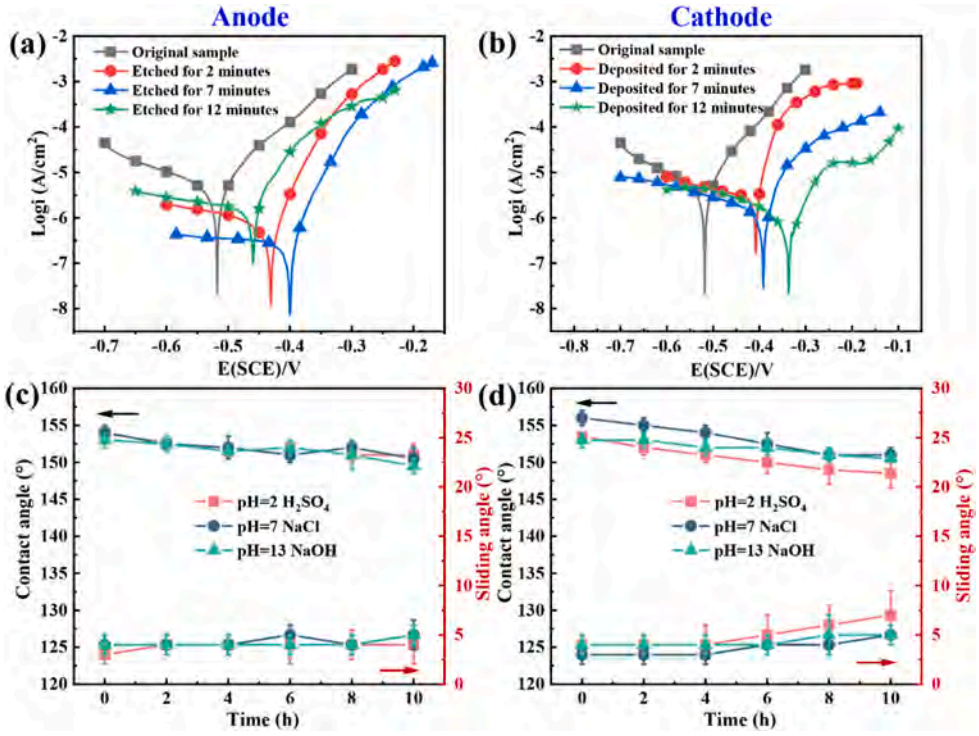

Fig. 6. Polarization curves: (a) Anode etching samples and (b) Cathode deposition samples; CA and SA after immersion: (c) Anode etching samples and (d) Cathode deposition samples.

morphology at 7 min (Fig. 3(g)) despite developing localized pit structures. Extended processing to 12 min primarily intensified pit depth without altering the fundamental composite architecture (Fig. 3(h)). The persistent micro-nano topography, coupled with PTES modification-induced surface energy reduction, facilitates stable air cushion formation upon water contact, accounting for the consistent superhydrophobicity despite structural evolution. Comprehensive analysis integrating morphological evolution with CA/SA measurements from both electrodes conclusively identifies 7 min as the optimal electrochemical processing duration.

Fig. 4 presents the XRD patterns of electrochemically processed anode and cathode specimens. The anode specimen exhibited characteristic diffuse scattering superimposed with sharp Cu (PDF 04–0836) crystalline peaks [17], indicative of retained amorphous matrix architecture with localized crystallization of metallic copper. In contrast, the cathode counterpart demonstrated exclusively sharp Cu diffraction signatures, suggesting a surface composition dominated by crystalline Cu phases without detectable amorphous components. The different characteristic structures of the anode and cathode specimens make them exhibit different properties in the subsequent physical property characterization.

Fig. 5 delineates the surface compositional evolution of electrochemically processed specimens through XPS analysis, with EDS elemental mapping confirming oxide presence on both electrodes - a finding consistent with XPS results (Fig. S1–S2). The anode survey spectrum (Fig. 5(a)) identified five principal elements: Zr, Al, Cu, C, and O. High-resolution spectra revealed: (i) Zr 3d doublet at 182.1 eV and 184.6 eV corresponding to ZrO_2 [18] (Fig. 5(b)); (ii) Cu 2p spectrum with Cu^{2+} signatures at 934.5 eV (Cu $2p_{3/2}$) and 954.6 eV (Cu $2p_{1/2}$) for CuO, accompanied by Cu^{+} peaks at 932.5 eV and 952.4 eV for Cu_2O, along with satellite features at 943.8 eV and 962.2 eV characteristic of CuO [19] (Fig. 5(c)); (iii) Al 2p peak at 75.9 eV indicative of Al_2O_3 [20] (Fig. 5(d)); (iv) O 1s showing three components at 530.2 eV (O^{2-}), 531.7 eV (OH^{-}), and 532.9 eV (H_2O) [21] (Fig. 5(e)). This collective evidence confirms anode surface oxidation forming ZrO_2-CuO--Cu_2O-Al_2O_3 composite oxides.

Conversely, cathode surface analysis (Fig. 5(f–i)) demonstrated distinct chemistry dominated by Cu, Fe, O, and C. The Cu 2p spectrum exhibited characteristic peaks at 934.3 eV (Cu $2p_{3/2}$) and 954.4 eV (Cu $2p_{1/2}$) for CuO, with additional Cu_2O signatures at 932.4 eV/952.4 eV and CuO satellite features at 943.8 eV/962.2 eV [19] (Fig. 5(g)). Fe 2p spectrum revealed Fe^{3+} oxidation states at 710.5 eV (Fe $2p_{3/2}$) and 724.1 eV (Fe $2p_{1/2}$) corresponding to Fe_2O_3 [22] (Fig. 5(h)). Oxygen speciation analysis (Fig. 5(i)) displayed binding energies at 529.7 eV (O^{2-}), 531.5 eV (OH^{-}), and 533.6 eV (H_2O) [21], collectively confirming cathode formation of Cu_2O-CuO-Fe_2O_3 composite oxides during electrodeposition.

The XPS findings collectively demonstrate distinct electrochemical reaction pathways: anodic oxidation during electrochemical etching involves electron loss from Al, Zr, and Cu atoms under applied potential, generating Al^{3+}, Zr^{4+}, Cu^{2+}, and Cu^{+} ions. Subsequently, hydrolysis and hydroxylation take place in alkaline electrolyte, eventually forming ZrO_2, Al_2O_3, Cu_2O, and CuO surface oxides. The cathodic reduction during electrodeposition facilitates the sequential reduction-oxidation of Cu^{2+} and Fe^{3+} ions through reaction with hydroxyl groups and dissolved oxygen, ultimately producing metallic Cu along with Cu_2O, CuO, and Fe_2O_3 composite oxides. This process was further enhanced by the alkaline environment's high OH^{-} concentration, which promoted oxide precipitation through both electrostatic stabilization of metal hydroxides and accelerated oxygen-involved redox kinetics. As attested by the

Table 1
Electrochemically fitted parameters and corrosion resistance efficiency of different samples.

Processing methods	i_{corr} (A/cm^2)	E_{corr} (V)	η (%)
original sample	4.38×10^{-6}	−0.52	0
Etching for 2 min	6.67×10^{-7}	−0.42	84.65
Etching for 7 min	2.54×10^{-7}	−0.40	94.20
Etching for 12 min	1.52×10^{-6}	−0.45	65.12
Deposition for 2 min	2.29×10^{-6}	−0.40	46.51
Deposition for 7 min	1.38×10^{-6}	−0.39	67.90
Deposition for 12 min	1.32×10^{-6}	−0.34	69.30

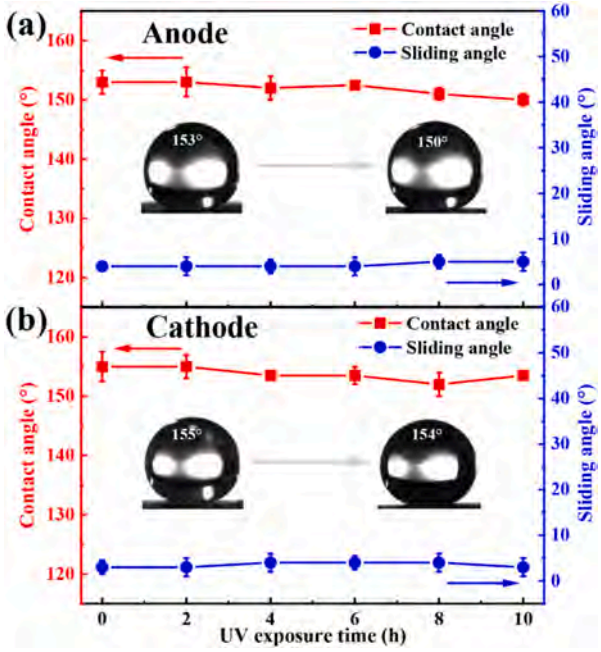

Fig. 7. CAs and SAs of the superhydrophobic samples after UV irradiation: (a) Anode and (b) Cathode.

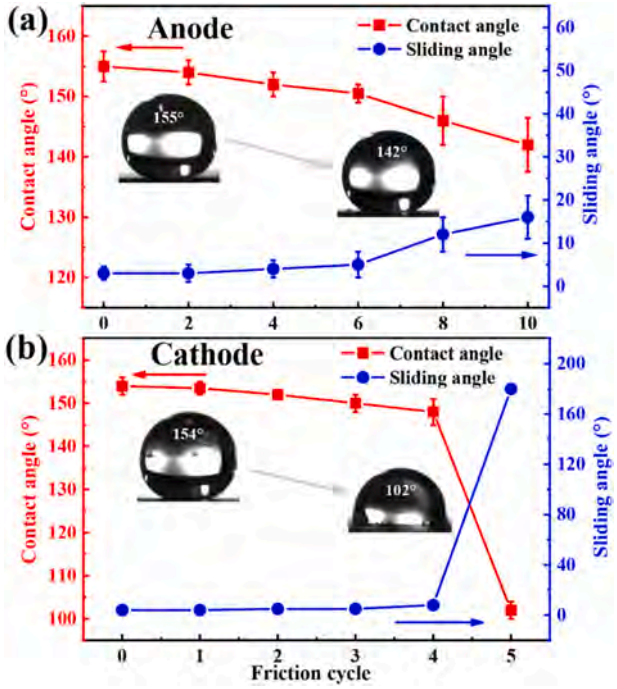

Fig. 8. CAs and SAs of the superhydrophobic samples after the mechanical test: (a) Anode and (b) Cathode.

oxide phases identified by XPS, this rationalizes the surface oxidation pathways observed in both electrodes.

3.2. Surface structure stability

3.2.1. Corrosion resistance

The corrosion resistance of superhydrophobic surfaces is of critical importance for their practical deployment in complex service environments. Initial electrochemical evaluations were performed in aqueous 3.5 wt% NaCl solution, with Fig. 6(a)–(b) presenting the polarization curves of modified cathode and anode specimens after electrochemical treatment, respectively, while Table 1 summarizes the corrosion parameters (corrosion potential E_{corr}, corrosion current density i_{corr}, and corrosion resistance efficiency η. Among them η=(i_0-i_{corr})/i_0, i_0 is the corrosion current density of MG.) derived through Tafel extrapolation. For anodically etched specimens (Fig. 6(a)), the icorr values demonstrated a decrease followed by an increase as a function of etching duration. This trend was inversely correlated with the evolution of E_{corr} and reached a peak at a processing time of 7 min. At this critical duration, the anode specimen exhibited optimal corrosion resistance characteristics with $E_{corr} = -0.40$ V, $i_{corr} = 2.54 \times 10^{-7}$ A/cm^2, and η = 94.20 %, representing a substantial reduction in corrosion rate compared to untreated substrates. Cathode specimens demonstrated comparatively stable corrosion resistance across deposition times (Fig. 6 (b)), consistently surpassing the performance of pristine MG. The 7 min cathodically deposited specimen attained $E_{corr} = -0.40$ V with $i_{corr} = 1.38 \times 10^{-6}$ A/cm^2 and η = 67.90 %, indicating synchronized optimization of surface hydrophobicity and corrosion resistance. Crucially, both anode and cathode samples attained peak anti-corrosion performance when subjected to 7 min electrochemical treatment, demonstrating this duration constitutes the optimal equilibrium between structural modification and surface protection.

To evaluate practical corrosion resistance under service conditions, systematic immersion testing was implemented by submerging superhydrophobic anode and cathode specimens in H_2SO_4 (pH = 2), NaCl (pH = 7, 3.5 wt%), and NaOH (pH = 13) solutions for extended durations, with concurrent monitoring of CA and SA. Fig. 6(c) demonstrates that anode specimens maintained robust superhydrophobicity across all environments, retaining CAs>150° and SAs<5° throughout testing. Notably, stable non-wettability under strongly acidic (pH = 2) and alkaline (pH = 13) conditions confirms effective barrier functionality against corrosive ion penetration. Cathode specimens exhibited pH-dependent behavior, preserving CAs>150° in neutral/alkaline media but displaying gradual CA reduction in acidic environments (Fig. 6(d)). Both electrode specimens demonstrated significantly enhanced corrosion resistance compared to untreated MG, attributable to a dual protection mechanism combining air-trapping micro-nano structures and in-situ formed oxide passivation layers.

3.2.2. UV resistance and mechanical stability

Given that photocatalytic materials are generally susceptible to UV-induced deactivation, the UV resistance of the superhydrophobic structures on the electrodes was evaluated. As shown in Fig. 7, the wettability hardly deteriorated under prolonged UV irradiation. Specifically, within a 10-h irradiation period, the CA of the anode sample decreased from 153° ± 2°–150° ± 2°, and that of the cathode sample decreased from 155° ± 2.5°–154° ± 2.5° and the SA remained below 5.5°. These results confirm that both electrode samples exhibit excellent UV resistance, attributed to the photostable surface fluorosilane layer, which effectively protects the hierarchical micro-nano structures from photon-induced structural degradation.

The wear resistance was evaluated by reciprocating sliding tests on SiC sandpaper at a normal load of 2 kPa and a length of 40 cm per cycle, revealing different wear behaviors among the superhydrophobic structures of different electrodes. As shown in Fig. 8, the anode sample maintained superhydrophobicity (CA = 150.5° ± 1.5°) for 6 cycles (total sliding 240 cm) and changed to a hydrophobic state (CA = 142° ± 4.5°) after 10 cycles (400 cm), indicating that the amorphous matrix as the oxide carrier of the hierarchical structure has excellent mechanical durability. The cathode sample, however, showed faster degradation, with CA decreasing from 154° ± 2°–148° ± 3° after 4 cycles (160 cm) and further dropping to 102° ± 2° after 5 cycles (200 cm), due to the delamination of the coating exposing the underlying MG substrate. The disparity in wear resistance originating from the fundamental architectural differences - the anode surface is structurally reinforced by the

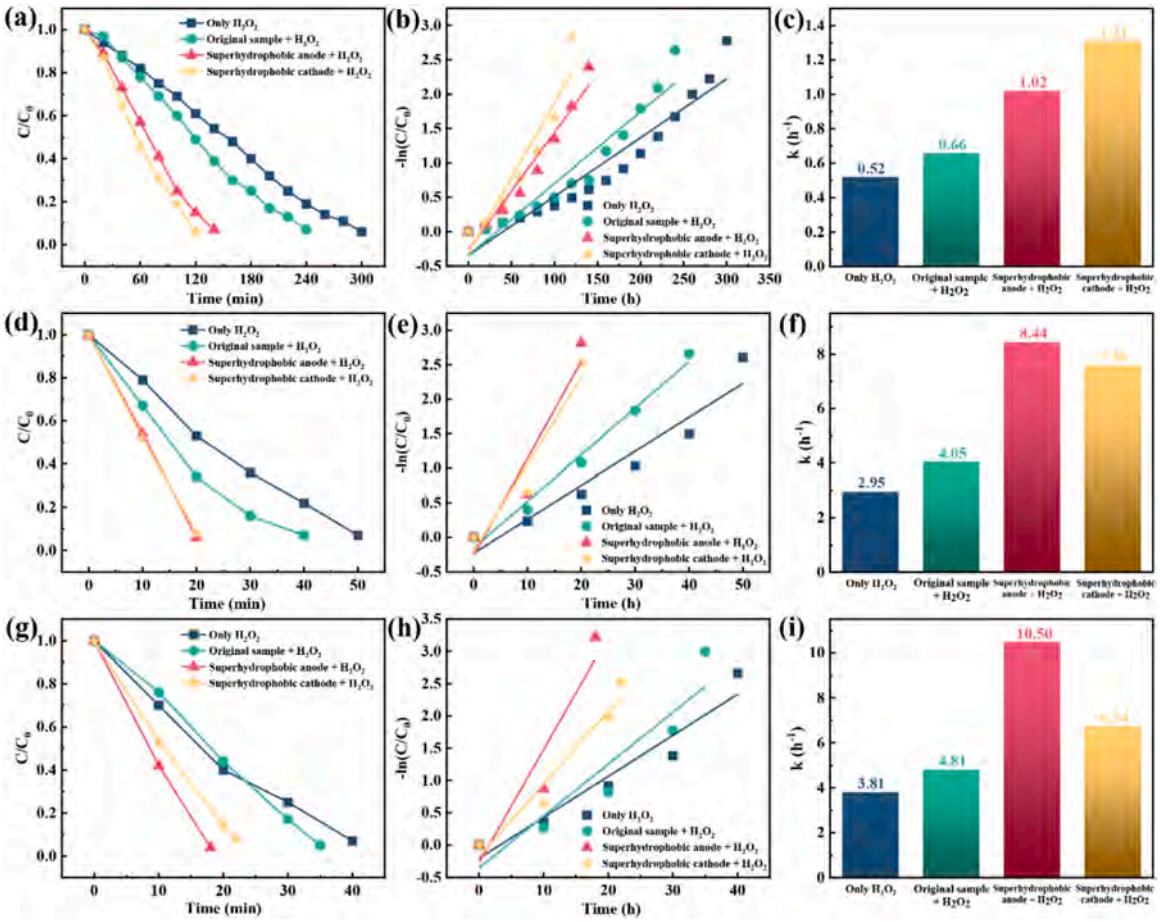

Fig. 9. Degradation efficiencies of different samples in MO solutions using different light sources: (a) Degradation curves for visible light; (b) Pseudo-first-order curves for visible light; (c) Apparent rate constants for visible light; (d) Degradation curves for UV–visible light; (e) Pseudo-first-order curves for UV–visible light; (f) Apparent rate constants for UV–visible light; (g) Degradation curves for UV light, (h) Pseudo-first-order curves for UV light; (i) Apparent rate constants for UV light.

integrity of the bulk metallic glass, while the cathode coating has interfacial fragility.

3.3. Photocatalytic degradation

3.3.1. Characteristics and mechanism

The structure analysis results show that multiple oxides are distributed on the superhydrophobic surfaces of the anode and cathode. Among these composed oxides, ZrO_2 is a semiconductor with a relatively wide bandgap and can exhibits photocatalytic effects under UV irradiation [23]. Cu_2O [24], CuO [25], and Fe_2O_3 [26] have narrower bandgaps and display photocatalytic activity under visible light irradiation. Therefore, Mott-Schottky tests were conducted on the superhydrophobic surfaces of the anode and cathode (the results are presented in Fig. S3). Both the anode and cathode curves have positive slopes, indicating that they are both n-type semiconductors. The flat band potential of the anode is −0.10 eV, and the flat band potential of the cathode is −0.19 eV. It can be simply estimated from the flat band potential that the conduction potential of both the anode and cathode is more negative than the redox potential of $\bullet O_2^-$ [27]. Photogenerated electrons on superhydrophobic surfaces can spontaneously reduce O_2 to $\bullet O_2^-$. Here, to verify the photocatalytic effect of the superhydrophobic surfaces of the anode and cathode, the photocatalytic degradation of MO is used as the reaction model to investigate the photocatalytic degradation activity upon irradiation by three light sources: visible light (400–780 nm) (Fig. 9(a)–(c)), UV–visible light (350–780 nm) (Fig. 9(d)–(f)), and UV light (300–400 nm) (Fig. 9(g)–(i)). The intensity of each light source is the same, and the pristine MG is the control group, while the blank control group is formed by adding H_2O_2.

Fig. 9(a) shows the degradation curves of different samples upon irradiation by visible light (400–780 nm). When only H_2O_2 is added, the degradation rate of MO decreases gradually with irradiation time, attaining 90 % after 300 min. After the addition of the MG sample, the degradation rate of the solution decreases at a slightly higher rate compared to the blank control group, achieving more than 90 % at 240 min. After the addition of the superhydrophobic anode and cathode samples, MO in the solution is degraded completely (>95 %) within 140 min for the anode and within 120 min for the cathode. The curves of the pseudo-first-order kinetics model and the bar diagrams of the apparent rate constants are plotted in Fig. 9(b)–(c) according to the Langmuir-Hinshelwood model [27]. The apparent rate constants of the MO degradation reactions by the anode and cathode are 1.02 and 1.31, respectively, which are significantly higher than 0.52 and 0.66 when only H_2O_2 and MG are added.

Fig. 9(d) presents the degradation curves under UV–visible light (350–780 nm) irradiation. When only H_2O_2 is added to the MO solution, MO breakdowns within 50 min. When MG is incorporated, the degradation time diminishes to 40 min. After the addition of the superhydrophobic anode and cathode, the degradation efficiency is even better, with MO degraded completely within 20 min. The pseudo-first-order kinetics curve and apparent rate constants are shown in Fig. 9 (e)–(f). Compared with visible light exposure, UV–visible light illumination produces better results.

Further experiments are carried out to explore the photocatalytic

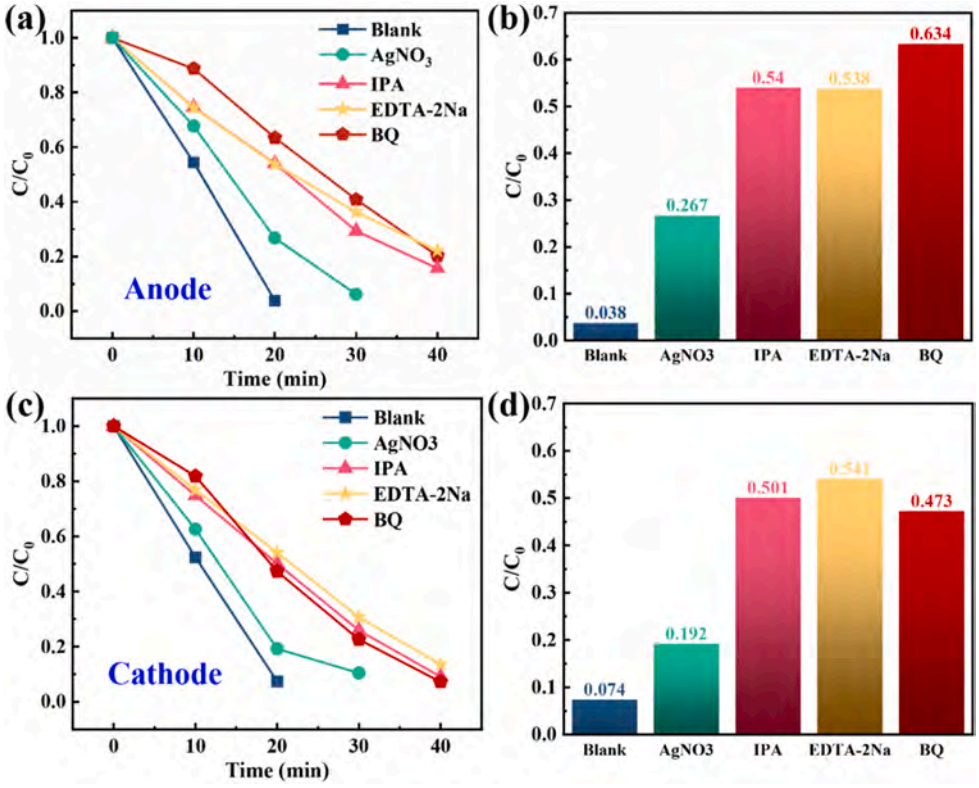

Fig. 10. Effects of free radical quenchers on the degradation efficiency of superhydrophobic samples.

degradation characteristics of different samples upon irradiation by 300~400 nm light (Fig. 9(g)–(i)). Under UV light irradiation, the photocatalytic degradation efficiency is generally enhanced as UV accelerates the decomposition of H_2O_2 into ·OH. Nevertheless, the degradation rate of the cathode decreases instead because of the response of multiple oxides to light.

In comparison with commonly used materials for MO degradation, the catalytic material developed in this study demonstrates good performance under visible light and neutral conditions: the apparent rate constant of the anode is comparable to that of g-C_3N_5 and superior to g-C_3N_4, while the degradation effectiveness of the cathode exceeds that of both g-C_3N_5 and g-C_3N_4 [28]. Under UV–visible light conditions, the apparent rate constants of both the anode and cathode are close to those of Fe-based amorphous ribbons such as $Fe_{73.5}Si_{13.5}B_9Cu_1Nb_3$, but lower than those of compositions like $Fe_{78}Si_9B_{13}$ [29]. It should be noted that Fe-based amorphous ribbons require acidic conditions for degradation, whereas this study was conducted entirely under neutral conditions. Although different catalysts have different applicable conditions, making direct comparisons inappropriate, acidic conditions may cause secondary pollution in water bodies and limit practical application scope. Therefore, the multifunctional bulk catalytic material developed in this study not only performs well but also offers higher environmental compatibility, showing certain application potential.

It is widely acknowledged that photogenerated electrons (e^-), holes (h^+), hydroxyl radicals (·OH), and superoxide radicals ($\cdot O_2^-$) are involved in photocatalytic reactions [30]. To clarify the role of active

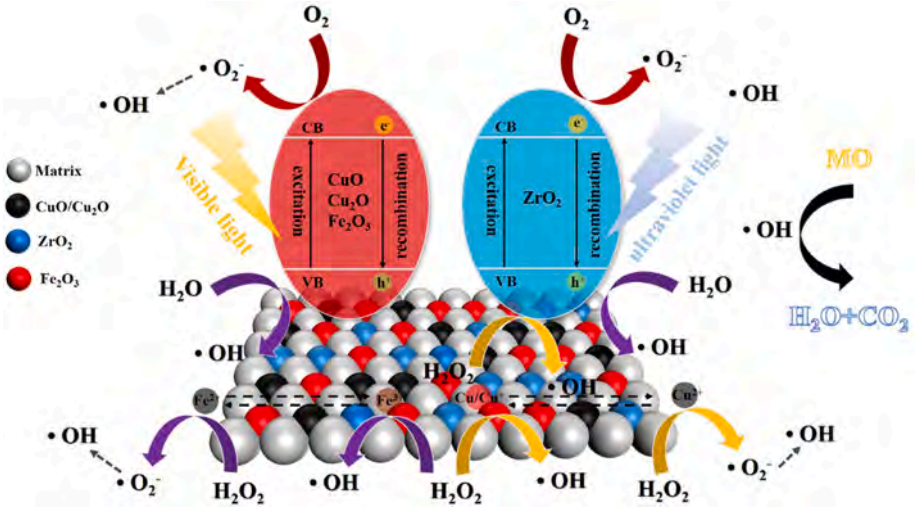

Fig. 11. Degradation mechanism of MO on superhydrophobic surfaces.

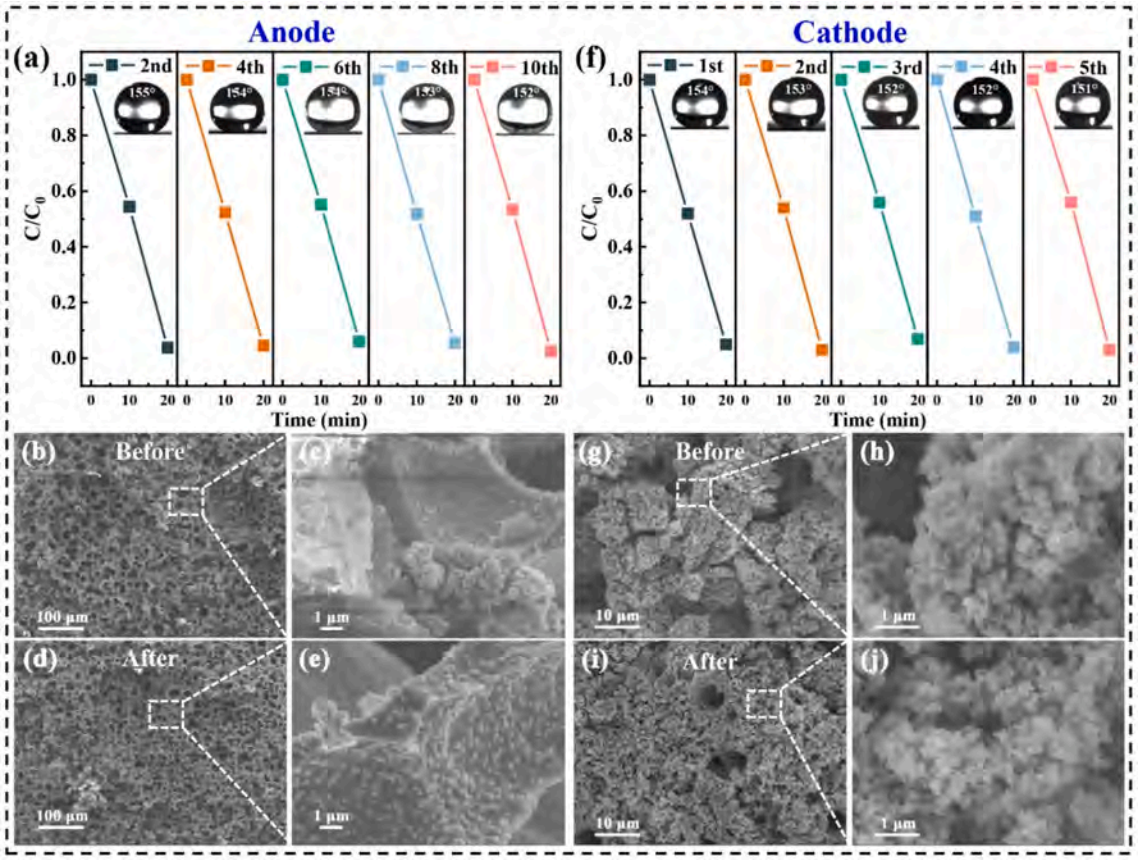

Fig. 12. Cyclic degradation efficiency and CAs: (a) Anode and (f) Cathode; Surface morphologies: (b)–(c) Anode before cycling; (d)–(e) Anode after cycling; (g)–(h) Cathode before cycling; (i)–(j) Cathode after cycling.

substances under ultraviolet–visible light irradiation, $AgNO_3$, disodium ethylenediaminetetraacetate (EDTA-2Na), benzoquinone (BQ), and isopropanol (IPA) are employed as quenchers to capture e^-, h^+, $\cdot O_2^-$, and ·OH, respectively. Fig. 10(a) shows the degradation curves of the superhydrophobic anode after the addition of different free radical quenchers, and Fig. 10(b) shows the extent of degradation of the superhydrophobic anode during 20 min degradation in the presence of different quenchers. Fig. 10(c)–(d) display the degradation curves and apparent rate constants of the cathode after 20 min with the addition of different quenchers. It can be observed that the effects of the anode and cathode are similar. The degradation rates of all the systems decrease after the addition of quenchers. Among them, the impact of $AgNO_3$ on

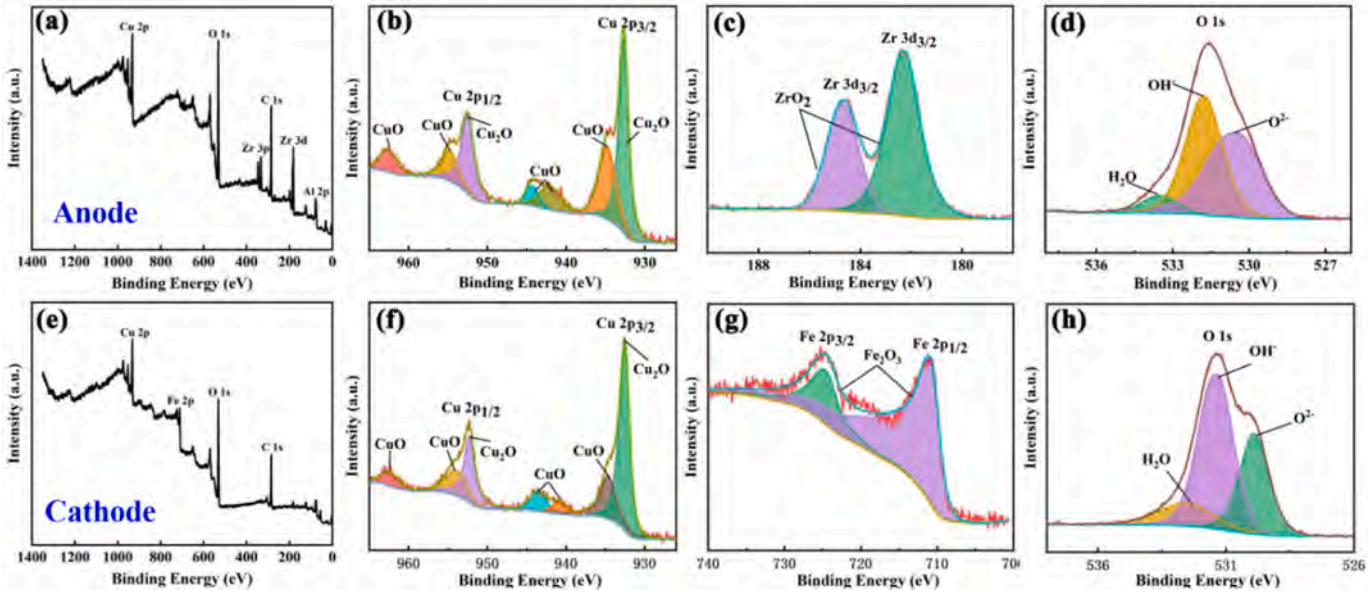

Fig. 13. XPS spectra of the anode after cycling: (a) Survey spectrum; (b) Cu 2*p*; (c) Zr 3*d*; (d) O 1*s*; (e) O 1*s*; XPS spectra of the anode: (e) Survey spectrum, (f) Cu *2p*, (g) Fe 2*p*, and (h) O 1*s*.

the degradation rate is slightly smaller, while IPA, EDTA-2Na, and BQ have a greater influence on the degradation efficiency. The results suggest that the degradation mechanisms of the anode and cathode samples are essentially the same, with e^-, h^+, $\cdot O_2^-$, and ·OH playing significant roles and $\cdot O_2^-$ having the greatest influence on the degradation rate.

Based on the above experimental results, the photocatalytic mechanisms exposed to different light sources are proposed. Under visible light irradiation, the oxides on the superhydrophobic surface, such as CuO, Cu_2O, and Fe_2O_3, are sensitive to visible light thus generating e^- and h^+ to react with H_2O_2 to yield ·OH and $\cdot O_2^-$. $\cdot O_2^-$ further reacts with H_2O_2 to generate ·OH. Ultimately, ·OH oxidizes MO into inorganic small molecules [31,32]. On the other hand, Cu, Cu^+, Cu^{2+}, and Fe^{3+} on the superhydrophobic sample undergo the Fenton-like reaction with H_2O_2 to produce ·OH and $\cdot O_2^-$ and accelerate degradation [33]. Moreover, rapid transfer of photogenerated e^- mitigates the recombination of e^- and h^+ to enhance the catalytic efficiency. During exposure to ultraviolet light, ZrO_2 on the superhydrophobic sample has photocatalytic activity, while under the influence of ultraviolet light, H_2O_2 decomposes to form ·OH to accelerate the degradation of organic substances. The photocatalytic degradation mechanism of MO on the surface of the superhydrophobic structure is described in Fig. 11 [33–38].

3.3.2. *Cyclic degradation stability*

The service life of the photocatalytic surfaces is of great significance in applications. Here, under the irradiation of UV–visible light (350–780 nm), the cyclic stability pertaining to MO degradation on the cathode and anode samples is evaluated. Fig. 12(a) indicates that after 10 degradation cycles, the superhydrophobic anode maintains good stability, with the surface CA being above 152° and the degradation efficiency remaining stable. As shown in Fig. 12(f), the superhydrophobic cathode also maintains good stability for 5 cycles, showing a superhydrophobic state and no obvious decline in the catalytic efficiency.

To understand the structural variations of superhydrophobic surfaces after cyclic degradation, the surface morphologies of the samples after multiple cycles are observed using SEM. As shown in Fig. 12(b)–(e), the superhydrophobic anode exhibits essentially no change before and after cycling, in addition to no obvious traces of corrosion, indicative of excellent stability. Fig. 12(g)–(j) shows that the surface micro-nanostructure of the superhydrophobic cathode remains stable before and after cycling without damage and showing the intact cauliflower structure. Moreover, as shown in Fig. S8, the EDS patterns are similar before and after cycling. Fig. 13(a) shows that the anode surface after cycling has the same Zr, Al, Cu, C, and O concentrations. Fig. 13(b)–(d) provides confirmation that the composition is similar before and after cycling, and Fig. 13(e)–(h) shows no obvious changes corroborating the stability. The above results demonstrate that both the anode and cathode samples have good cyclic stability and can cope with complex application environments.

The antibacterial properties of the anode and cathode samples are determined and the details can be found in the supplementary materials.

4. Conclusion

Electrochemical processing combining electrochemical etching and electrochemical deposition is performed on $Zr_{46}Cu_{46}Al_8$ MG to improve the structure and properties. The superhydrophobic structures on the anode and cathode have not only excellent photocatalytic activity but also outstanding corrosion resistance, mechanical stability, and ultraviolet resistance. The anode fabricated by electrochemical etching shows a surface contact angle of 155°. It has a honeycomb-like micro-nanometer structure mainly composed of $Cu/ZrO_2/CuO/Cu_2O$. The cathode surface produced by electrochemical deposition has a contact angle of 154° with the cauliflower-like micro-nano multi-level structure containing primarily $Cu/CuO/Cu_2O/Fe_2O_3$. The superhydrophobic cathode and anode have outstanding corrosion resistance. The current corrosion density of the anode is 2.54×10^{-7} A/cm^2, and the corrosion resistance efficiency is 94.2 %. The corrosion current density of the cathode is 1.38×10^{-6} A/cm^2, and the corrosion resistance efficiency is 67.9 %. Moreover, both the cathode and anode are stable after immersion in acidic, alkaline, and salt solutions for over 10 h. Their corrosion resistance is far superior to that of untreated metallic glass. Both the superhydrophobic cathode and anode have remarkable photocatalytic activity. Under UV–visible light irradiation, they are capable of completely degrading the methyl orange solution within 20 min, and the cycling stability is also excellent. The results reveal a novel strategy to improve the surface structure and properties of metallic glasses and expand their commercial viability.

CRediT authorship contribution statement

Guanzhong Ding: Writing – original draft, Methodology, Investigation. **Guoyang Zhang:** Writing – review & editing, Writing – original draft, Supervision, Investigation. **Ranfeng Wei:** Writing – review & editing, Writing – original draft. **Yujia Wang:** Writing – original draft. **Rui Zheng:** Writing – original draft. **Qijing Sun:** Writing – review & editing. **Jingwang Lv:** Writing – review & editing. **Haipeng Wang:** Writing – review & editing. **Dan Li:** Writing – review & editing. **Paul K. Chu:** Writing – review & editing. **Li Liu:** Writing – review & editing, Supervision, Resources. **Xiangjin Zhao:** Writing – review & editing, Supervision, Resources, Conceptualization.

Declaration of competing interest

The authors declare that they have no known competing financial interests or personal relationships that could have appeared to influence the work reported in this paper.

Acknowledgments

This work was supported by the National Natural Science Foundation of China (No. 51871191), Shandong Provincial Natural Science Fund for Excellent Young Scientists Fund Program (Overseas) (No. 2024HWYQ-074), Natural Science Foundation of Shandong Province (Nos. ZR2019MEM044, ZR2023QE213 and ZR2023QE056), City University of Hong Kong Donation Research Grants (DON-RMG 9229021 and 9220061), as well as Guangdong - Hong Kong Technology Cooperation Funding Scheme (TCFS, GHP/212/22GD and CityU 9440399).

Appendix A. Supplementary data

Supplementary data to this article can be found online at https://doi.org/10.1016/j.intermet.2025.109009.

Data availability

Data will be made available on request.

References

[1] R. Wei, R. Zheng, C. Li, W. Wang, H. Zhang, Q. Sun, J. Lv, G. Zhang, L. Liu, X. Zhao, ZrO_2 superhydrophobic coating with an excellent corrosion resistance and stable degradation performance on Zr-based bulk metallic glass, Materials 17 (2023) 118, https://doi.org/10.3390/ma17010118.

[2] R. Zheng, R. Wei, C. Li, H. Zhang, W. Wang, H. Wang, Q. Sun, J. Lv, G. Zhang, X. Zhao, L. Liu, Preparation of superhydrophobic surface on Zr-based bulk metallic glasses with excellent photocatalytic properties, Colloids Surf., A 701 (2022) 134946, https://doi.org/10.1016/j.colsurfa.2024.134946.

[3] M. Zhang, Y.J. Wang, G.Z. Ding, R. Zheng, R.F. Wei, G.Y. Zhang, Q.J. Sun, X. J. Zhao, L. Liu, Biocompatible superhydrophobic surface on Zr-based bulk metallic glass: fabrication, characterization, and biocompatibility investigations, Ceram. Int. 49 (2023) 25549–25562, https://doi.org/10.1016/j.ceramint.2023.05.095.

[4] Z. Jia, X.G. Duan, P. Qin, W.C. Zhang, W.M. Wang, C. Yang, H.Q. Sun, S.B. Wang, L. C. Zhang, Disordered atomic packing structure of metallic glass: toward ultrafast

hydroxyl radicals production rate and strong electron transfer ability in catalytic performance, Adv. Funct. Mater. 27 (2017) 1702258, https://doi.org/10.1002/Adfm.201702258.
[5] J.Q. Wang, Y.H. Liu, M.W. Chen, D.V. Louzguine-Luzgin, A. Inoue, J.H. Perepezko, Excellent capability in degrading azo dyes by MgZn-based metallic glass powders, Sci. Rep. 2 (2012) 418, https://doi.org/10.1038/Srep00418.
[6] J.W. Chen, L. Ji, Z.G. Zheng, X. Liu, Z.G. Qiu, S.H. Zhou, L. Huang, J. Wei, D. C. Zeng, Improving the degradation efficiency for the azo dye of $Fe_{82}Si_{2.5}B_{12}P_{2.5}C$ alloy via heat treatment, Mater. Lett. 300 (2021) 130187, https://doi.org/10.1016/J.Matlet.2021.130187.
[7] Z. Lv, Y. Yan, C. Yuan, B. Huang, C. Yang, J. Ma, J. Wang, L. Huo, Z. Cui, X. Wang, W. Wang, B. Shen, Making Fe-Si-B amorphous powders as an effective catalyst for dye degradation by high-energy ultrasonic vibration, Mater. Des. 194 (2020) 108876, https://doi.org/10.1016/j.matdes.2020.108876.
[8] X.D. Qin, Z.W. Zhu, G. Liu, H.M. Fu, H.W. Zhang, A.M. Wang, H. Li, H.F. Zhang, Ultrafast degradation of azo dyes catalyzed by cobalt-based metallic glass, Sci. Rep. 5 (2016) 18226, https://doi.org/10.1038/Srep18226.
[9] Z. Deng, C. Zhang, L. Liu, Chemically dealloyed MgCuGd metallic glass with enhanced catalytic activity in degradation of phenol, Intermetallics 52 (2014) 9–14, https://doi.org/10.1016/j.intermet.2014.03.007.
[10] C. Yang, C. Zhang, L. Liu, Excellent degradation performance of 3D hierarchical nanoporous structures of copper towards organic pollutants, J. Mater. Chem. A 6 (2018) 20992–21002, https://doi.org/10.1039/c8ta07973k.
[11] S.L. Zhu, J. Jiang, X.B. Zhang, Y.Q. Liang, Z.D. Cui, X.J. Yang, Novel nanosized anatase TiO_2 hexagonal prism filled with nanoporous structure, Mater. Des. 116 (2017) 238–245, https://doi.org/10.1016/j.matdes.2016.12.017.
[12] S.S. Wang, L. Liu, Fabrication of novel nanoporous copper powder catalyst by dealloying of ZrCuNiAl amorphous powders for the application of wastewater treatments, J. Hazard. Mater. 340 (2017) 445–453, https://doi.org/10.1016/j.jhazmat.2017.07.022.
[13] C.J. Yang, Y.C. Zhao, Y.L. Tian, F.J. Wang, X.P. Liu, X.B. Jing, Fabrication and stability investigation of bio-inspired superhydrophobic surface on nitinol alloy, Colloids Surf., A 567 (2019) 16–26, https://doi.org/10.1016/j.colsurfa.2019.01.032.
[14] Y. Xu, M.M. Hassan, S. Ali, H. Li, Q. Ouyang, Q. Chen, Self-cleaning-mediated SERS chip coupled chemometric algorithms for detection and photocatalytic degradation of pesticides in food, J. Agric. Food Chem. 69 (2021) 1667–1674, https://doi.org/10.1021/acs.jafc.0c06513.
[15] T. Singh, A. Dvivedi, Developments in electrochemical discharge machining: a review on electrochemical discharge machining, process variants and their hybrid methods, Int. J. Mach. Tool Manufact. 105 (2016) 1–13, https://doi.org/10.1016/j.ijmachtools.2016.03.004.
[16] S. Ge-Zhang, H. Yang, H. Ni, H. Mu, M. Zhang, Biomimetic superhydrophobic metal/nonmetal surface manufactured by etching methods: a mini review, Front. Bioeng. Biotechnol. 10 (2022) 958095, https://doi.org/10.3389/fbioe.2022.958095.
[17] T.A. Formentini, I. Basile-Doelsch, S. Legros, A.J. Frierdich, A. Pinheiro, C.V. S. Fernandes, F.J.K. Mallmann, D. Borschneck, M. Da Veiga, E. Doelsch, Copper (cu) speciation in organic-waste (OW) amended soil: instability of OW-borne Cu(I) sulfide and role of clay and iron oxide minerals, Sci. Total Environ. 848 (2022) 157779, https://doi.org/10.1016/j.scitotenv.2022.157779.
[18] C. Caravaca, L. Shi, S. Balvay, P. Rivory, E. Laurenceau, Y. Chevolot, D. Hartmann, L. Gremillard, J. Chevalier, Direct silanization of zirconia for increased biointegration, Acta Biomater. 46 (2016) 323–335, https://doi.org/10.1016/j.actbio.2016.09.034.
[19] B.K. Singh, A. Shaikh, R.O. Dusane, S. Parida, Copper oxide nanosheets and nanowires grown by one-step linear sweep voltammetry for supercapacitor application, J. Energy Storage 31 (2020) 101631, https://doi.org/10.1016/j.est.2020.101631.
[20] J. Haeberle, K. Henkel, H. Gargouri, F. Naumann, B. Gruska, M. Arens, M. Tallarida, D. Schmeisser, Ellipsometry and XPS comparative studies of thermal and plasma enhanced atomic layer deposited Al_2O_3-films, Beilstein J. Nanotechnol. 4 (2013) 732–742, https://doi.org/10.3762/bjnano.4.83.
[21] M.M. Wang, Q.H. Shu, Y.S. Shi, C.L. Teng, J.F. Wang, S.H. Jin, S.S. Chen, J.F. Qin, D.X. Wang, Fabrication of hydrophobic AlCoCrFeNi high-entropy alloy and superior corrosion resistance to NTO aqueous solution, J. Alloys Compd. 915 (2022) 165394, https://doi.org/10.1016/j.jallcom.2022.165394.
[22] Z. Ni, C. Zhang, Z.Q. Wang, S. Zhao, X.Y. Fan, H.Z. Jia, Performance and potential mechanism of transformation of polycyclic aromatic hydrocarbons (PAHs) on various iron oxides, J. Hazard. Mater. 403 (2021) 123993, https://doi.org/10.1016/j.jhazmat.2020.123993.
[23] N.S. Hassan, A.A. Jalil, A review on self-modification of zirconium dioxide nanocatalysts with enhanced visible-light-driven photodegradation of organic pollutants, J. Hazard. Mater. 423 (2022) 126996, https://doi.org/10.1016/j.jhazmat.2021.126996.
[24] W. Wang, H.M. Feng, J.G. Liu, M.T. Zhang, S. Liu, C. Feng, S.G. Chen, A photo catalyst of cuprous oxide anchored MXene nanosheet for dramatic enhancement of synergistic antibacterial ability, Chem. Eng. J. 386 (2020) 124116, https://doi.org/10.1016/J.Cej.2020.124116.
[25] Z. Lin, J. Xiao, L. Li, P. Liu, C. Wang, G. Yang, Nanodiamond-embedded p-type copper(I) oxide nanocrystals for broad-spectrum photocatalytic hydrogen evolution, Adv. Energy Mater. 6 (2015) 1501865, https://doi.org/10.1002/aenm.201501865.
[26] L. Wang, T. Kumeria, A. Santos, P. Forward, M.F. Lambert, D. Losic, Iron oxide nanowires from bacteria biofilm as an efficient visible-light magnetic photocatalyst, ACS Appl. Mater. Interfaces 8 (2016) 20110–20119, https://doi.org/10.1021/acsami.6b06486.
[27] X.C. Lv, D.Y.S. Yan, F.L.Y. Lam, Y.H. Ng, S.M. Yin, A.K. An, Solvothermal synthesis of copper-doped BiOBr microflowers with enhanced adsorption and visible-light driven photocatalytic degradation of norfloxacin, Chem. Eng. J. 401 (2020) 126012, https://doi.org/10.1016/J.Cej.2020.126012.
[28] S. Liu, Y. Bu, S. Cheng, T. Yang, W. Hong, Preparation of g-C_3N_5/g-C_3N_4 heterojunction for methyl orange photocatalytic degradation: mechanism analysis, J. Water Process Eng. 54 (2023) 104019, https://doi.org/10.1016/j.jwpe.2023.104019.
[29] Z. Jia, J. Kang, W.C. Zhang, W.M. Wang, C. Yang, H. Sun, D. Habibi, L.C. Zhang, LC zhang surface aging behaviour of Fe-based amorphous alloys as catalysts during heterogeneous photo Fenton-like process for water treatment, Appl. Catal. B Environ. 204 (2017) 537–547, https://doi.org/10.1016/j.apcatb.2016.12.001.
[30] C.Q. Xu, D.Z. Li, X.L. Liu, R.Z. Ma, N. Sakai, Y.C. Yang, S.Y. Lin, J.L. Yang, H. Pan, J. Huang, T. Sasaki, Direct Z-scheme construction of g-C_3N_4 quantum dots/TiO_2 nanoflakes for efficient photocatalysis, Chem. Eng. J. 430 (2022) 132861, https://doi.org/10.1016/j.cej.2021.132861.
[31] M.Y. Zhu, D.H. Meng, C.J. Wang, J. Di, G.W. Diao, Degradation of methylene blue with H_2O_2 over a cupric oxide nanosheet catalyst, Chin. J. Catal. 34 (2013) 2125–2129, https://doi.org/10.1016/S1872-2067(12)60717-7.
[32] Y. Nie, C. Hu, L. Zhou, J. Qu, An efficient electron transfer at the Fe^0/iron oxide interface for the photoassisted degradation of pollutants with H_2O_2, Appl. Catal., B 82 (2008) 151–156, https://doi.org/10.1016/j.apcatb.2008.01.019.
[33] B.W. Zhao, H.L. Li, X.D. Qin, Z.K. Li, S.M. Zhang, A.M. Wang, H.F. Zhang, Z. W. Zhu, Performance enhancement and catalytic mechanism identification of Cu-based composite for degradation of organic contaminants, Powder Technol. 389 (2021) 11–20, https://doi.org/10.1016/j.powtec.2021.04.092.
[34] M.H. Pérez, L.P. Vega, H. Zúñiga-Benítez, G.A. Peñuela, Comparative degradation of alachlor using photocatalysis and photo-fenton, water, Air, Soil Pollut 229 (2018) 346, https://doi.org/10.1007/S11270-018-3996-6.
[35] J.Q. You, X.H. Zhang, J.L. Chen, Degradation of antibiotics by fenton-like reaction catalyzed by iron oxide, Adv. Mater. Sci. Eng. 2023 (2022) 6849818, https://doi.org/10.1155/2022/6849818.
[36] A.B. Rezaie, M. Montazer, M.M. Rad, Environmentally friendly low cost approach for nano copper oxide functionalization of cotton designed for antibacterial and photocatalytic applications, J. Clean. Prod. 204 (2018) 425–436, https://doi.org/10.1016/j.jclepro.2018.08.337.
[37] R. Vinayagam, B. Singhania, G. Murugesan, P.S. Kumar, R. Bhole, M. K. Narasimhan, T. Varadavenkatesan, R. Selvaraj, Photocatalytic degradation of methylene blue dye using newly synthesized zirconia nanoparticles, Environ. Res. 214 (2022) 113785, https://doi.org/10.1016/J.Envres.2022.113785.
[38] X. Fan, L. Peng, X. Wang, S. Han, L. Yang, H. Wang, C. Hao, Efficient capture of lead ion and methylene blue by functionalized biomass carbon-based adsorbent for wastewater treatment, Ind. Crop. Prod. 183 (2022) 114966, https://doi.org/10.1016/j.indcrop.2022.114966.

Supplementary Materials

Integrated Design of Superhydrophobic Structures and Photocatalytic Functions of $Zr_{46}Cu_{46}Al_8$ Metallic Glass Surfaces

Guanzhong Ding [a], Guoyang Zhang [b, *], Ranfeng Wei [b], Yujia Wang [a], Rui Zheng [a], Qijing Sun [b], Jingwang Lv [b], Haipeng Wang [b], Dan Li [c], Paul K. Chu [c], Li Liu [a, *], Xiangjin Zhao [b, *]

[a] School of Environmental and Material Engineering, Yantai University, Yantai 264005, China.

[b] Yantai Key Laboratory of Advanced Nuclear Energy Materials and Irradiation Technology, College of Nuclear Equipment and Nuclear Engineering, Yantai University, Yantai 264005, China.

[c] Department of Physics, Department of Materials Science and Engineering, and Department of Biomedical Engineering, City University of Hong Kong, Kowloon, Hong Kong, China

* Corresponding authors: Guoyang Zhang (zhangguoyang@ytu.edu.cn), Li Liu (liuli1980@ytu.edu.cn), Xiangjin Zhao (zl2915@ytu.edu.cn)

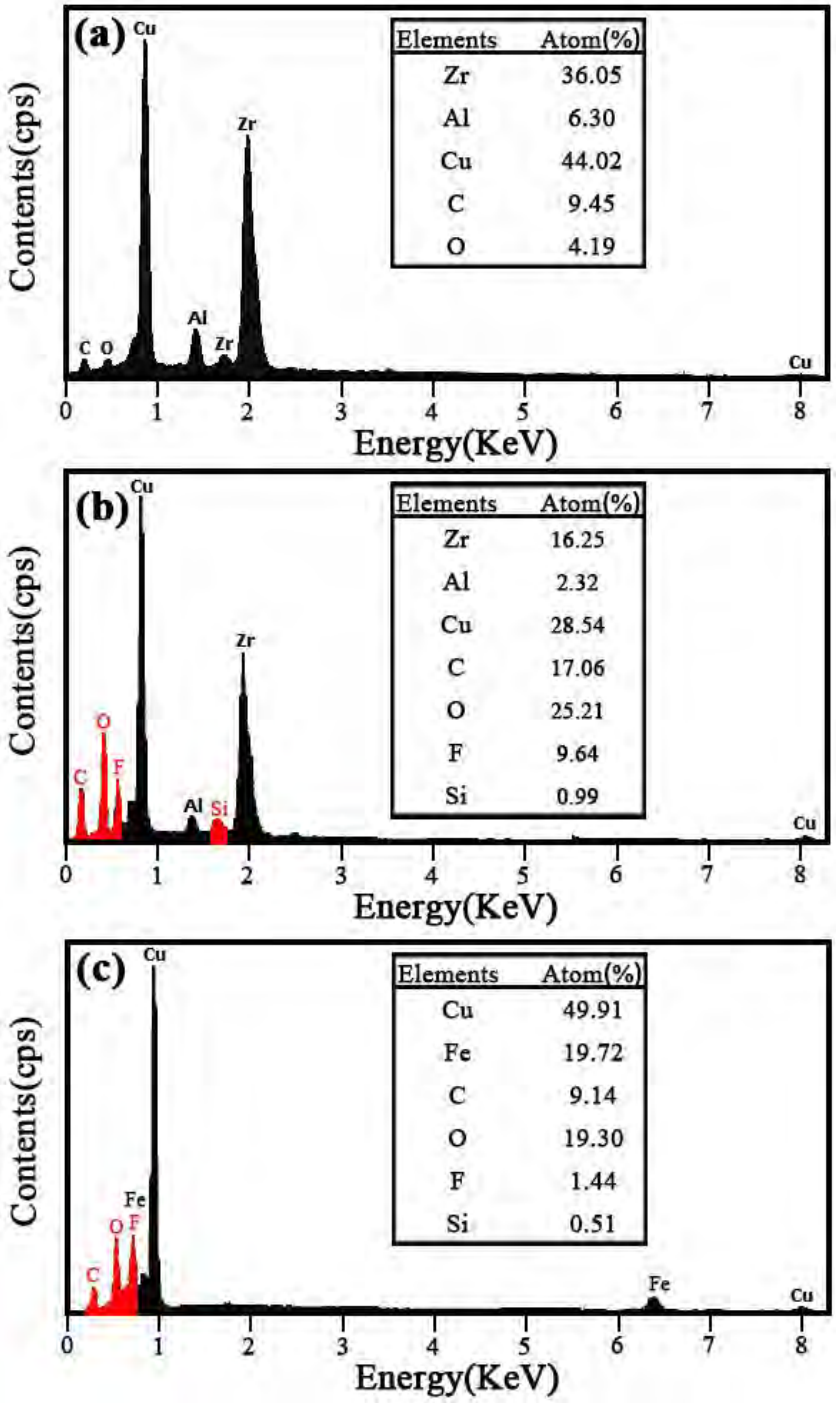

Fig. S1. EDS spectra of: (a) Pristine MG, (b) Anode, and (c) Cathode.

Table S1. Elemental composition of different samples (at%).

	Zr	Al	Cu	C	O	F	Si	Fe
Original sample	36.05	6.30	44.02	9.45	4.19	/	/	/
Anode sample	16.25	2.32	28.54	17.06	25.21	9.64	0.99	/
Cathode sample	/	/	49.91	9.14	19.30	1.44	0.51	/

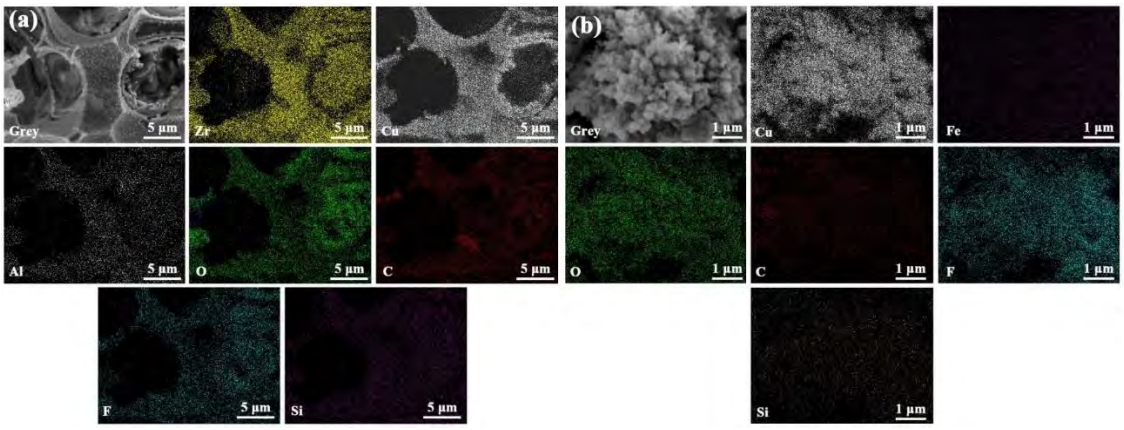

Fig. S2. Elemental maps of (a) Anode and (b) Cathode.

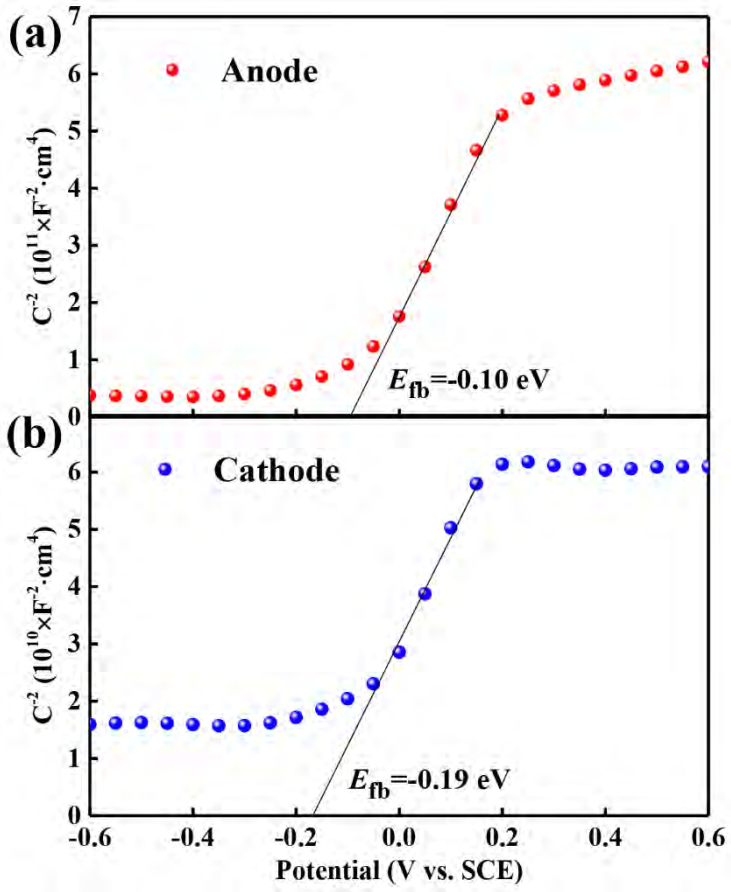

Fig. S3. Mott-Schottky curves of anode and cathode at optimal electrochemical processing time

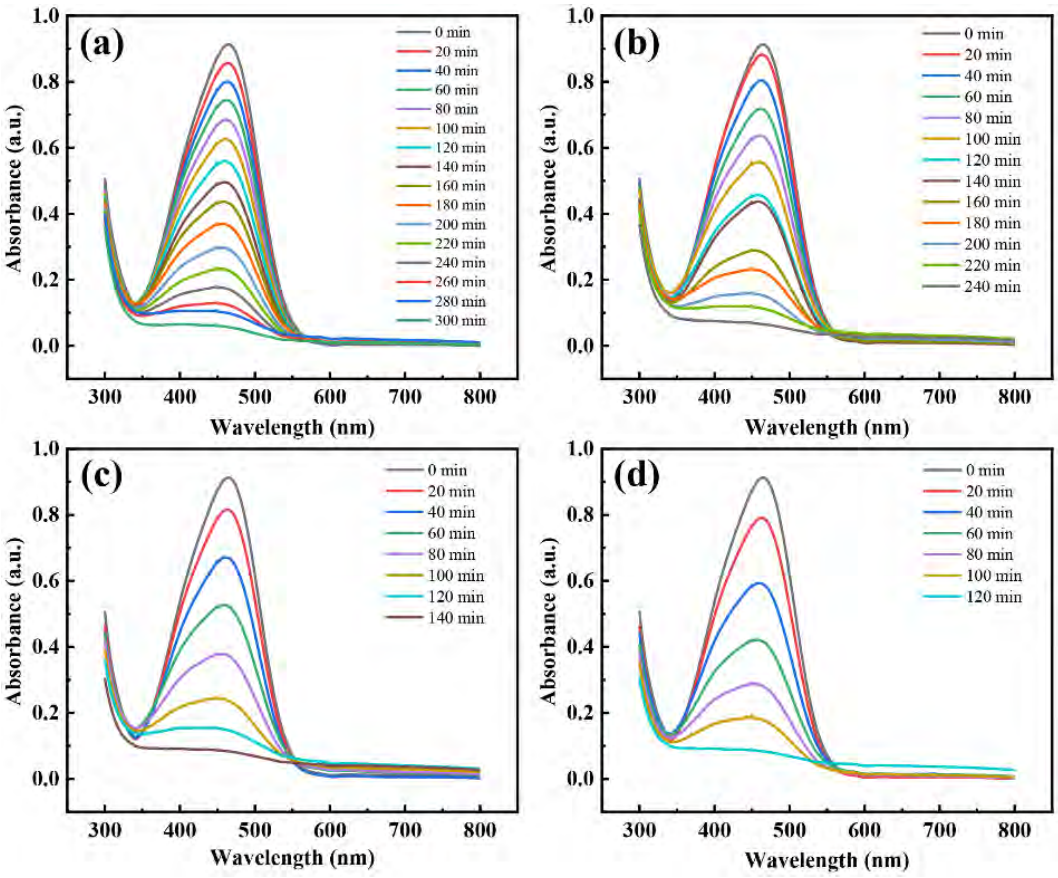

Fig. S4. Time-dependent UV spectra of the MO solution under visible light irradiation: (a) H_2O_2 only, (b) Original sample + H_2O_2, (c) Superhydrophobic anode + H_2O_2, and (d) Superhydrophobic cathode + H_2O_2.

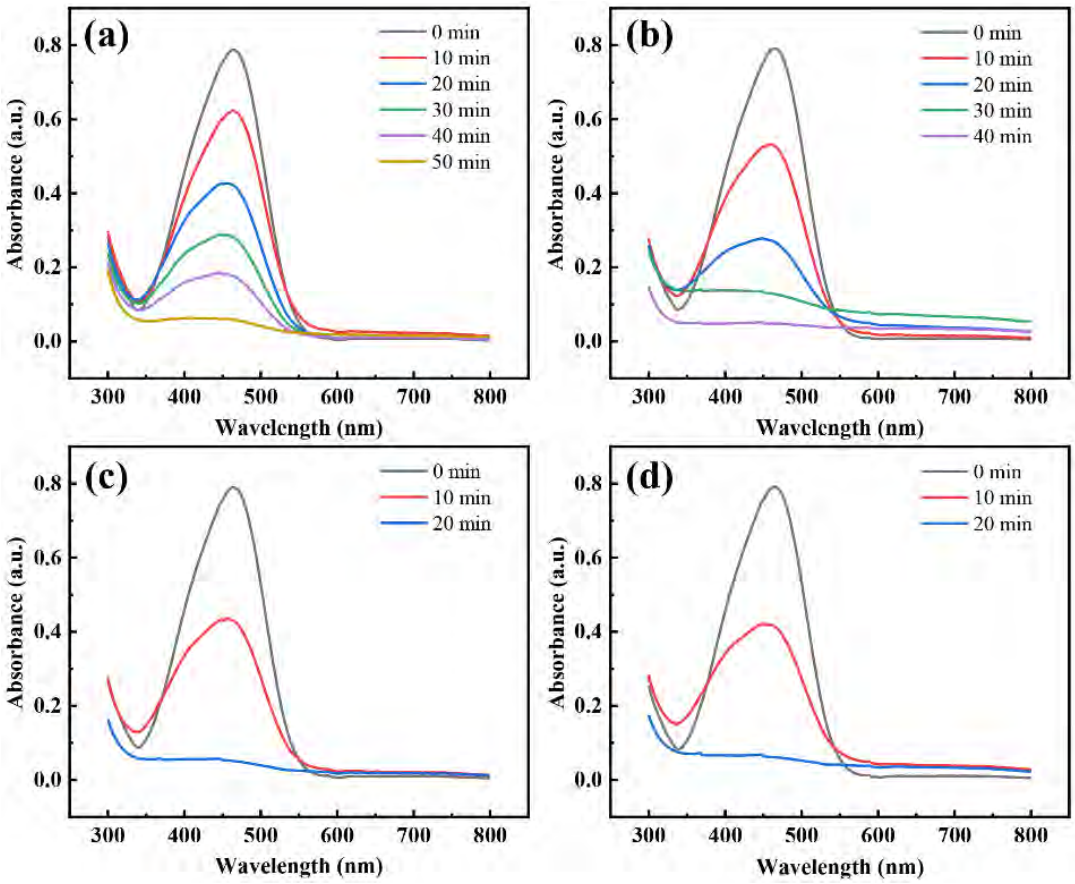

Fig. S5. Time-dependent UV spectra of the MO solution under UV-visible light irradiation: (a) H_2O_2 only, (b) Original sample + H_2O_2, (c) Superhydrophobic anode + H_2O_2, and (d) Superhydrophobic cathode + H_2O_2.

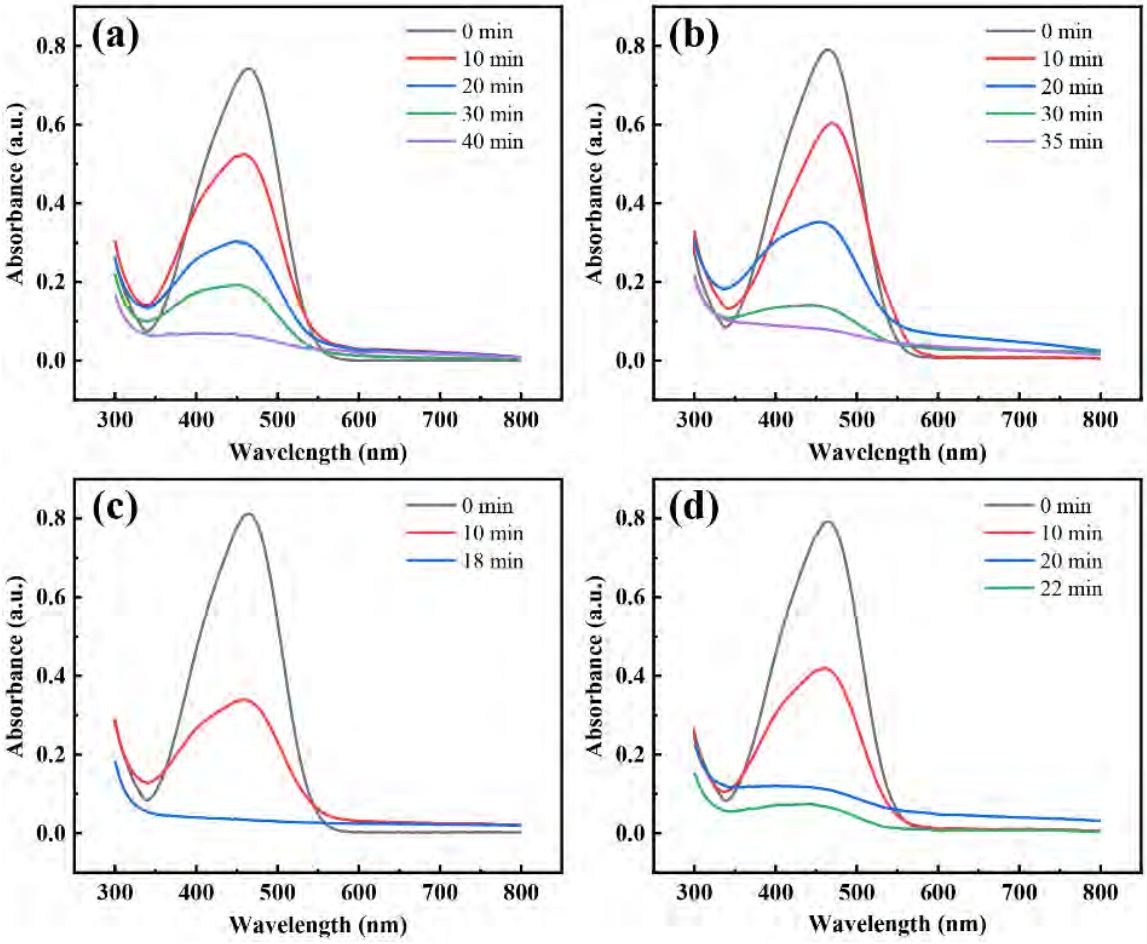

Fig. S6. Time-dependent UV spectra of the MO solution upon UV light illumination: (a) H_2O_2 only, (b) Original sample + H_2O_2, (c) Superhydrophobic anode + H_2O_2, and (d) Superhydrophobic cathode + H_2O_2.

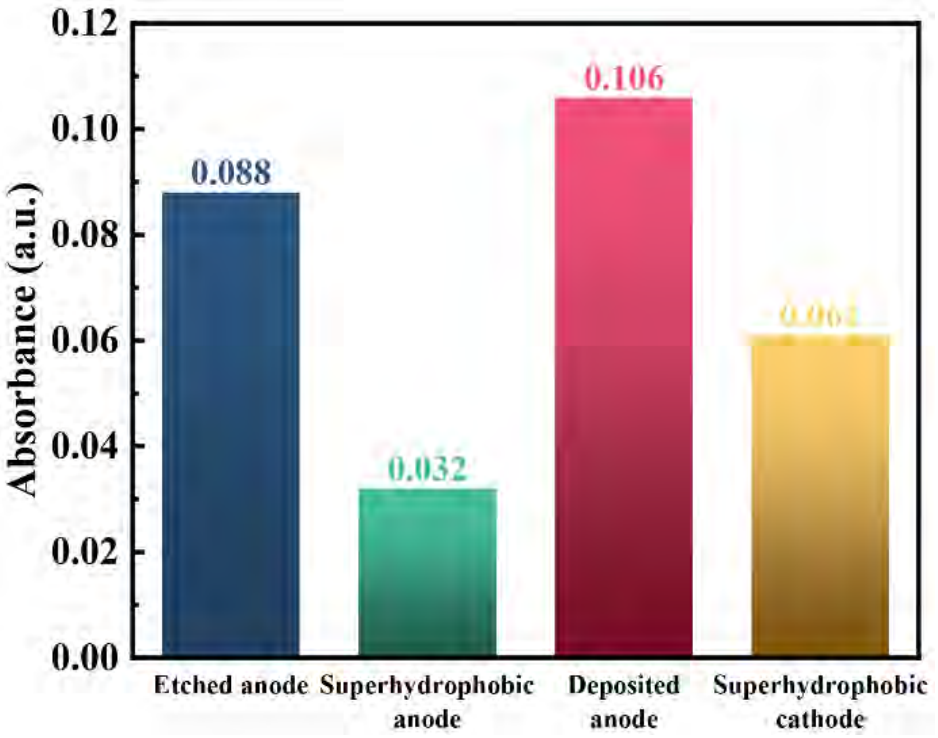

Fig. S7. Comparison of the degradation efficiency between unmodified samples and superhydrophobic samples.

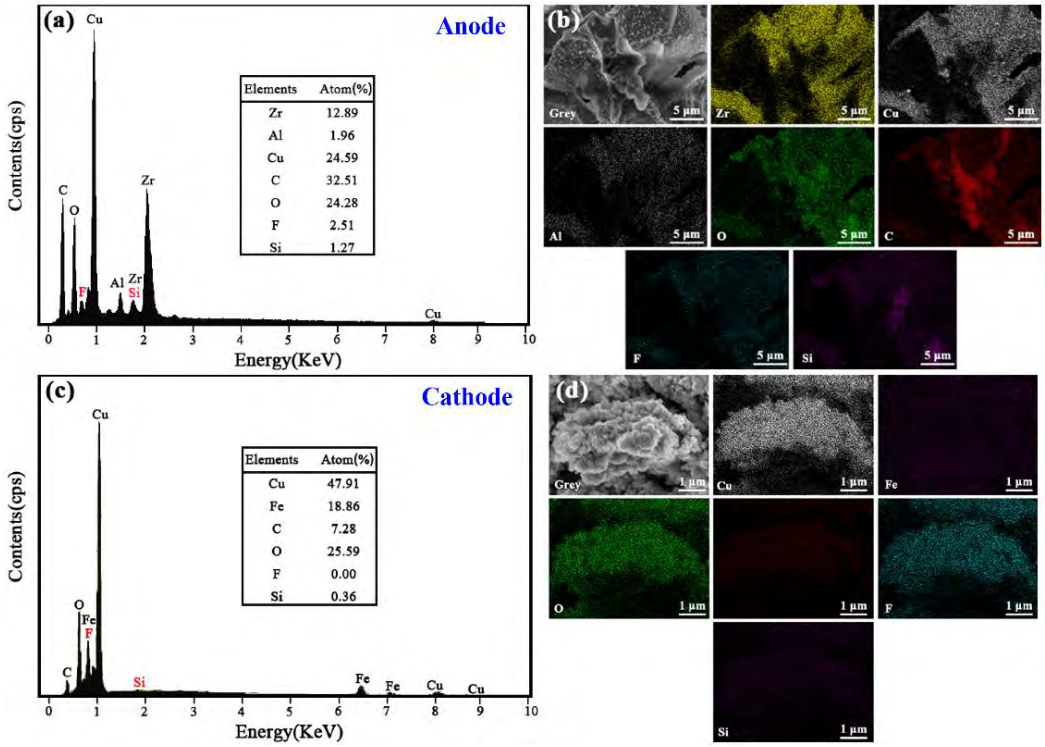

Fig. S8. EDS spectra and elemental maps of the surfaces after degradation: (a and b) Anode and (c and d) Cathode.

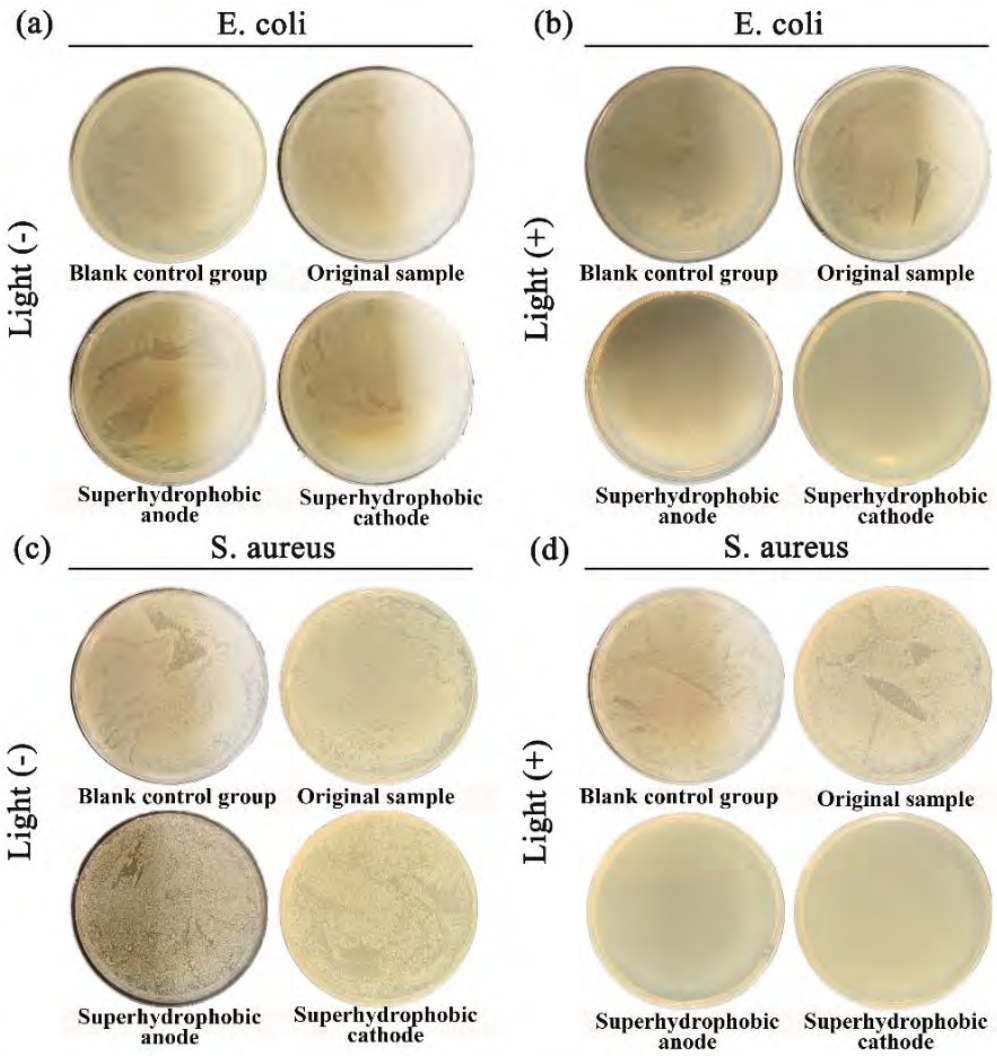

Fig. S9. Sterilization efficiency against Escherichia coli: (a) Light conditions and (b) Dark conditions; Sterilization efficiency against staphylococcus aureus: (c) Light conditions and (b) Dark conditions.